Available online at www.sciencedirect.com
ScienceDirect
Cement and Concrete Research 37 (2007) 1 – 12
Cement and Concrete Research

The nanogranular behavior of C-S-H at elevated temperatures (up to 700 °C)

Matthew J. DeJong, Franz-Josef Ulm *

Massachusetts Institute of Technology, Cambridge MA, USA

Received 14 February 2006; accepted 14 September 2006

Abstract

Cement-based materials are non-combustible, but the complex chemo-physical mechanisms that drive at elevated temperatures the thermal degradation of the mechanical properties (stiffness, strength) are still an enigma that have deceived many decoding attempts. This paper presents, for the first time, results from a new experimental technique that allows one to rationally assess the evolution of the nano-mechanical behavior of cement paste at elevated temperatures. Specifically, the thermal degradation of the two distinct calcium-silicate hydrate (C-S-H) phases, Low Density (LD) C-S-H and High Density (HD) C-S-H, is assessed based on a statistical analysis of massive nanoindentation tests. From a combination of nanoindentation, thermogravimetry and micromechanical modeling, we identify a new mechanism, the thermally induced change of the packing density of the two C-S-H phases, as the dominant mechanism that drives the thermal degradation of cementitious materials. We argue that this loosening of the packing density results from the shrinkage of C-S-H nanoparticles that occurs at high temperatures, most probably due to the loss of chemically bound water.

Keywords: C-S-H; Mechanical behavior; Nanoindentation; High temperature; Granular material; Packing density

1. Introduction

What drives the thermal damage of Portlandite cement materials when exposed to high temperatures? — This question has re-surfaced recently in the aftermath of several extreme events that highlighted the vulnerability of concrete tunnels and high rise buildings subjected to high temperatures caused by fire (see e.g. [1]). From an engineering science perspective, the question we raise here is motivated by a long and ongoing discussion in Concrete Science and Engineering. Currently, there are (at least) two schools of thought on the matter: one which considers that the thermal damage of cement-based materials, i.e. the irreversible loss of strength and stiffness due to high temperature exposure, is dominated by microcracking induced by the thermal mismatch (different stiffness, thermal dilatation, etc.) of some meso-scopic properties (see e.g. [2]) and interfaces (see e.g. [3]). This school of thought has its merit as to the macroscopic behavior of concrete. For example, it is believed that the difference in thermal dilatation coefficient between the aggregates and the cement paste matrix can cause considerable tension at the aggregate–matrix interface leading eventually to interface fracture (the classical quenching problem). Such purely mechanical effects, however, should play a diminishing role for cement pastes, for which high temperatures are known to detrimentally affect elasticity [4–6] and compressive strength [4,7]. The second school of thought attributes the thermal damage to the dehydration of the primary hydration products in hardened cement paste [8,9], namely the calcium-silicate-hydrates (C-S-H), occupying up to 70% by volume. This second school of thought owes much to the pioneering works of Harmathy, who by measuring dehydration using thermogravimetry, determined that the dehydration of C-S-H and Calcium Hydroxide (CH) are the primary physical origins of high temperature degradation [10,11]. It derives much of its conjectures from a combination of observed degradation of the macroscopic mechanical properties of hardened cement pastes, porosity measurements [7,5], and Scanning Electron Microscopy (SEM) images which show the effects of high temperature exposure on the microstructure [12,13].

* Corresponding author. Tel.: +1 617 2533544; fax: +1 617 2536044.
E-mail address: ulm@mit.edu (F.-J. Ulm).

0008-8846/$ - see front matter © 2006 Elsevier Ltd. All rights reserved.
doi:10.1016/j.cemconres.2006.09.006

Table 1
Composition of Type I OPC in mass percentage of each component as provided by the manufacturer

CaO	SiO_2	Al_2O_3	MgO	SO_3	Na_2O	Fe_2O_3	K_2O	C_3S	C_2S	C_3A
62.30	20.80	4.40	3.80	2.90	0.39	2.40	1.28	53.0	20.0	8.0

The focus of this paper is to use relatively new advances in nanotechnology to investigate the sources of high temperature degradation of cement paste at the nanoscale. In particular, we apply a recently developed statistical grid-nanoindentation technique [14] to thermally degraded materials to assess the residual mechanical properties of the two C-S-H phases that characterize cementitious materials [15–17]: Low Density (LD) C-S-H and High Density (HD) C-S-H. The experimental program and analysis techniques are presented first, followed by a presentation of the nanoindentation results. From a detailed micromechanics analysis we then identify the sources of the thermal degradation for both stiffness and strength properties of the C-S-H.

2. Experimental program

2.1. Materials and specimen preparation

Cement paste was prepared using Type I Portland cement (see Table 1) with a water–cement ratio of $w/c=0.5$. Specimens were cast in ~11 mm diameter cylindrical molds and vibrated at the time of casting to remove air bubbles. All specimens were removed from their molds within 7 days of casting and were immediately placed in lime water for curing. At an age of 28 days, after curing, specimens were cut into 10–14 mm long segments using a diamond saw. All cut surfaces were then sanded using two sandpapers of increasing fineness (grit), and then polished using four diamond suspension solutions with diamond particles of increasing fineness. Particle sizes in the diamond solutions ranged from 6.0 μm to 0.25 μm. After polishing, samples were placed in an ultrasonic bath to remove all dust and diamond particles. The control specimens (25 °C) were then tested in their saturated state and all other specimens were dried at 105 °C to effectively 'lock' their hydration state (at 28 days), i.e. to prevent further hydration. After drying, specimens were placed in a desiccator until further heating (or until testing in the case of the 105 °C test group).

Because the goal of this investigation is to determine material effects of high temperature exposure on cement paste, the heating procedure was selected to limit thermal gradients and therefore transient effects of heating. To accomplish this, specimens were heated at a rate of 1 K/min,[1] held at the desired maximum temperature for 24 h, and then cooled at a rate of 1 K/min. The temperatures included in this investigation were 25 °C, 105 °C, 200 °C, 300 °C, 400 °C, 550 °C, and 700 °C. After heating, specimens were again stored in desiccators at all times to prevent rehydration. Let us note that we also attempted to polish the samples immediately following heating (instead before heating) to eliminate the possibility of the surface roughness increasing during heating due to differential shrinkage or microcracking. However, sanding and polishing after heating was found to significantly degrade the surface and increase the roughness instead of making samples smoother. Therefore, polishing before heating was the only viable repeatable method.

[1] Heating was performed using a Barnstead FB1400 Furnace with a Eurotherm 2116 temperature controller which allowed programming of heating and cooling rates and the time of maximum temperature.

2.2. Thermogravimetry

Thermogravimetry (TG) is a technique which measures the mass change of a sample as a function of temperature. Thermal changes accompanying mass change in cementitious materials, such as dehydration, can be effectively measured using TG [10,18,19]. After curing, samples used for thermogravimetric analysis were cut from one indentation specimen. Samples were cut into cubes with a volume of approximately 5 mm^3, as required by the maximum allowable mass (50 mg) of the testing equipment (Perkin Elmer TGA7 Thermogravimetric Analyzer).

Thermogravimetric tests were performed on cement paste samples in a temperature range from ~20 °C (room temperature) to 1000 °C in three stages. First, the temperature was increased from 20 °C to 105 °C at a nominal rate of 5 K/min in order to remove all evaporable water from the sample. Second, the temperature was held constant at 105 °C for 60 min to ensure that all evaporable water was removed. Allowing the sample to reach equilibrium at 105 °C provides an effective division between the initial period of evaporation and the subsequent period of dehydration. Third, the temperature was increased from 105 °C to 1000 °C at a nominal rate of 5 K/min, during which dehydration occurred.

The results of the thermogravimetric analysis are shown in Fig. 1. The derivative of the mass loss clearly shows the primary range of C-S-H dehydration [10] between 105 °C and 300 °C, and the primary range of CH dehydration [10] between 400 °C and 600 °C. A secondary range of C-S-H dehydration between 650 °C and 800 °C which has been reported by Harmathy [10] is barely visible. Manual mass loss measurements for the indentation samples are also shown in Fig. 1 for comparison.

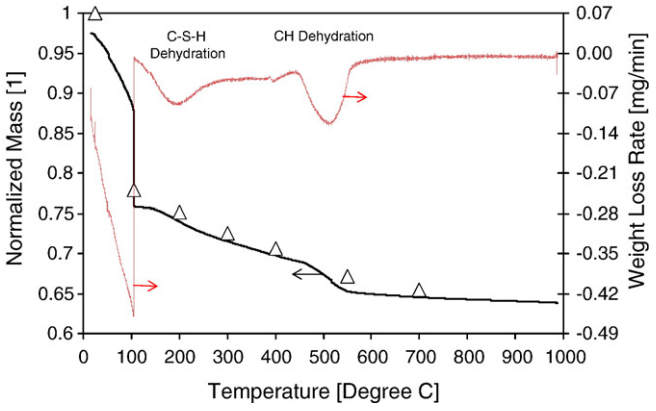

Fig. 1. Results of thermogravimetric analysis (TG) on $w/c=0.5$ cement paste. The normalized mass determined by TG (continuous line) is in excellent agreement with manual mass loss measurements of the specimens used for indentation (discrete points). The derivative of the weight loss (labeled 'weight loss rate') shows the characteristic C-S-H and CH dehydration.

2.3. Grid indentation technique

Methods for determining the mechanical properties of a material using indentation data are well established (for recent reviews, see [20,21]). The indentation technique consists of establishing contact between an indenter of known geometry and mechanical properties (typically diamond) and the indented material for which the mechanical properties are of interest, and subsequently acquiring the continuous change in penetration depth h as a function of increasing indentation load P (P–h curve, see Fig. 2). In particular, the extraction of mechanical properties is achieved by applying a *continuum scale* mechanical contact model to derive two quantities, indentation hardness H and indentation modulus M:

$$H \stackrel{def}{=} \frac{P}{A_c} \tag{1}$$

$$M \stackrel{def}{=} \frac{\sqrt{\pi}}{2}\frac{S}{\sqrt{A_c}} \tag{2}$$

All quantities required to determine H and M are directly obtained from the P–h curves, with the exception of the projected area of contact A_c. Chief among those are the maximum applied force P_{max}, corresponding maximum depth h_{max}, the unloading indentation stiffness $S=(dP/dh)_{h=h_{max}}$, and the residual indentation depth h_f of the material surface after full unloading (Fig. 2, curve (a)). The contact area A_c can also be extrapolated from the maximum depth h_{max} using the Oliver and Pharr method [22]. For homogenous material systems, the indentation modulus M can be linked to the elastic constants of the indented material by applying a linear elastic model to the data [23,24]. In the isotropic case, M reduces to the plane-stress elastic modulus,

$$M = \frac{E}{1-\nu^2} = 4G\frac{3K+G}{3K+4G} \tag{3}$$

where E is the Young's modulus, ν is the Poisson's ratio, G is the shear modulus and K is the bulk modulus of the indented isotropic material. Similarly, the hardness H can be related to strength properties, namely cohesion c and friction angle φ, and the cone angle θ [25] by:

$$H = c\mathcal{F}(\varphi,\theta) \tag{4}$$

where $\mathcal{F}(\varphi,\theta)$ is a dimensionless function.

The classical indentation methods are restricted to monolithic systems as the underlying indentation model assumes indentation into a homogeneous material half-space. Very recently, Constantinides and Ulm [14] extended the domain of application of this powerful technique to heterogenous multi-scale and multi-phase composite materials, a category composing the majority of solids, including cementitious materials. The experimental basis of this method is a large series of indentation tests carried out on a surface grid (grid indentation technique). Each indentation test is a single statistical event, and the mechanical properties extracted from continuum indentation analysis are considered as random variables. Those data are then analyzed by deconvoluting the empirical frequency densities or response distributions of the mechanical indentation properties, $x=(M, H)$, by means of a theoretical probability density function (PDF):

$$\text{For } x=(M,H) \text{ find } (\mu_J, s_J, f_J) \text{ from } \min \frac{1}{m}\sum_{i=1}^{m}(P_i - P(x_i))^2$$
$$\text{subjected to: } \sum_{J=1}^{n} f_J = 1 \tag{5}$$

where μ_J, s_J are the mean value and standard deviation of $x=(M, H)$ of phase $J=1$, n, and f_J is the volume fraction of this phase present in the heterogeneous material; P_i is the observed value of the experimental frequency density; m is the number of intervals (bins) chosen to construct the histogram, and $P(x_i)$ is the value of the theoretical probability density function at point x_I (assumed to be Gaussian):

$$P(x_i) = \sum_{J=1}^{n} \frac{f_J}{\sqrt{2\pi s_J^2}} \exp\left(-\frac{(x_i-\mu_J)^2}{2s_J^2}\right) \tag{6}$$

Let us note that there is no uniqueness of solution of the minimization problem (5). Some additional constraints help to constrain the possible solutions and ensure the repeatability of the automatized minimization process:

1. The minimization is done simultaneously for the indentation modulus M and the hardness H frequency distribution (minimization of the sum of the errors).
2. The minimization is done simultaneously for two different bin sizes (for both stiffness and hardness), which ensures that the deconvolution results are (almost) independent from the bin-size used to construct the histogram. These are for stiffness: $\Delta M=(2.5, 5.0)$ GPa; and for hardness $\Delta H=(110, 220)$ MPa. All bin-sizes satisfy the condition that the number of bins m is greater than the number of unknowns of the (H, M) deconvolution process, $5n-1$.

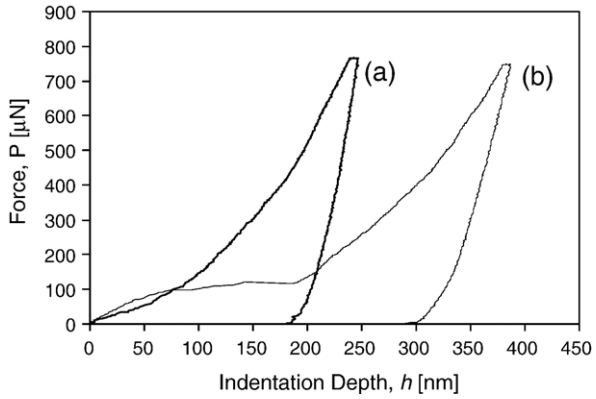

Fig. 2. Indentation response: indentation force P vs. indentation depth h. The regular curve (a) is a typical indentation curve for which the tools of continuum indentation analysis apply. In contrast, the irregular curve (b) exhibits a displacement jump in the force driven indentation tests, probably due to subsurface fracture.

3. In order to identify statistically relevant phase properties, the overlap of successive Gaussian curves representative of two phases is constrained by:

$$\mu_J + s_J \leq \mu_{J+1} - s_{J+1} \tag{7}$$

Fig. 3 shows a typical result of this deconvolution technique in the form of frequency plots of the indentation modulus and the indentation hardness obtained from 200 nanoindentation tests on the saturated control sample tested at 25 °C. For data modeling, $n=3$ phases were considered, which are, as we will see later on, (from left to right) the LD C-S-H phase, the HD C-S-H phase and Portlandite crystal.

The application of the continuum scale model to determine H, M from Eqs. (1) and (2) requires a careful monitoring of the maximum indentation depth h_{max}, which must be smaller than the characteristic size of the microstructure and larger than the characteristic size of the elementary particle. This can be summarized by the indentation scale separability condition [14]:

$$d \ll h_{max} \in [100, 300] \text{ nm} < \frac{D}{10} \tag{8}$$

where d and D stand for the characteristic size of the largest heterogeneity (particle size) of the indented material and of the microstructure, respectively. In the case of C-S-H, prime candidates for d are the single colloidal particle in C-S-H or the gel pores of similar size, $d \sim 5$ nm [16,26,27]. The characteristic size D of the microstructure of a well hydrated cement paste is on the order of $D \sim 1$–3 μm [19]; hence $h_{max} \in [100, 300]$ nm. For smaller depths, the indentation response will be affected by the discrete nature of the colloidal particles of C-S-H, and for larger depths the indentation response will be affected by the interaction of different phases of the microstructure. The order of magnitude of h_{max} also allows access to the in-situ properties of Portlandite (CH) and residual clinker phases if present. Indeed, the elementary size of the Portlandite crystal structure is on the order of $d=0.5$ nm and the size D of crystals present in cementitious materials is, on-average, of micrometer dimension.

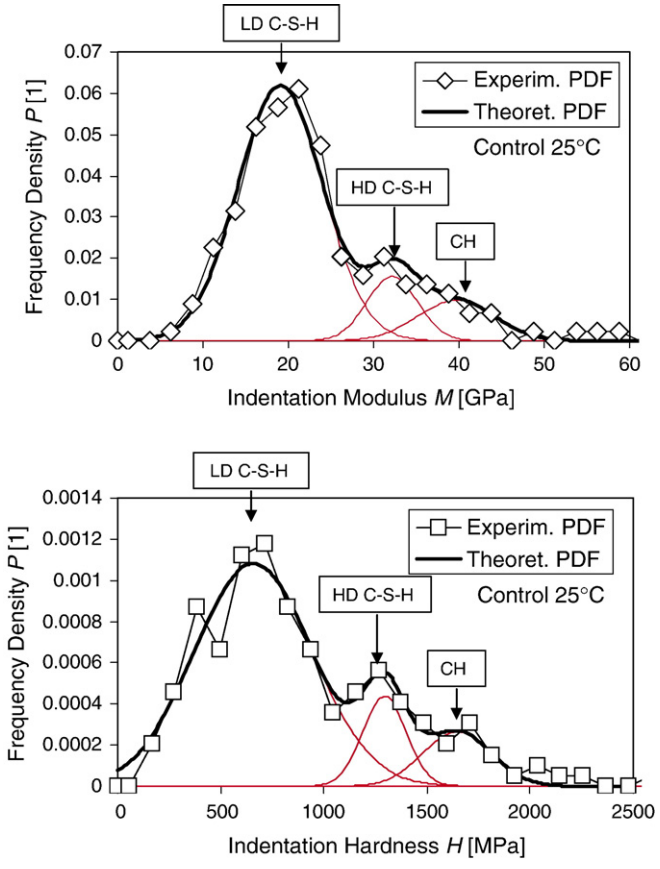

Fig. 3. Frequency plots of indentation modulus and indentation hardness with fitted Gaussian curves for low-density (LD) C-S-H, high-density (HD) C-S-H, and Portlandite (CH). The deconvolution was carried out for a bin size of $\Delta M=2.5$ GPa and $\Delta H=110$ MPa.

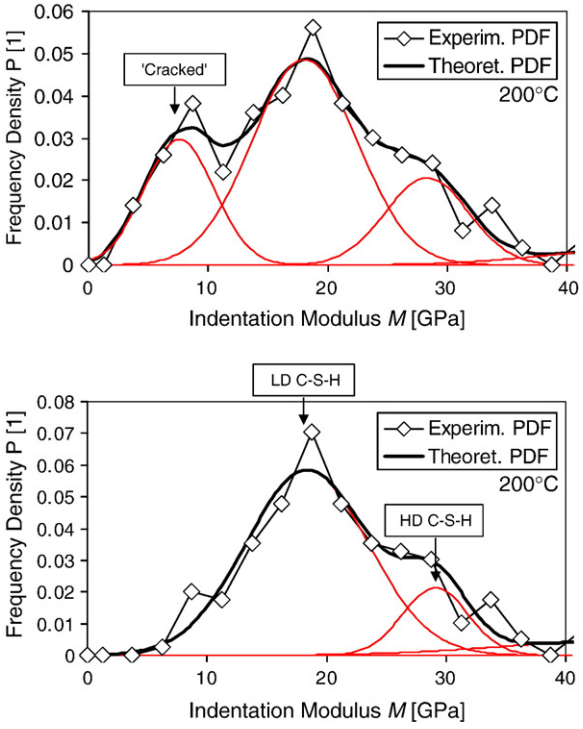

Fig. 4. Indentation modulus frequency plots: (top) without elimination of irregular (discontinuous) indentation data (200 data points); (bottom) after elimination of discontinuous data (160 data points).

Finally, a convenient way to achieve the target indentation depth in Eq. (8) is to employ a series of load-controlled indentation tests. This requires some experimental iteration. For the tested $w/c=0.5$ cement paste, we found that a maximum load of $P_{max}=650$–770 μN for the different investigation temperatures yields average maximum indentation depths in the desired range of 100–300 nm.

2.4. Data validation

The nanoindentation tests were conducted using the TriboIndenter (Hysitron, Inc.) in the NanoMechanical Technology Laboratory at MIT. Load and depth calibrations were measured and applied as suggested by the manufacturer of the equipment used. In all indentation tests, a trapezoidal load

Table 2
Summary of experimental nanoindentation program

Temp. [°C]	Number of tests		P_{max} [μN]		h_{max} [nm]	
	Total	Used	Mean	St.dev.	Mean	Stdev.
25	200	177	771	8	193	52
105	200	156	770	9	186	46
200	200	160	774	8	178	52
300	200	179	770	12	205	81
400	200	146	771	10	202	69
550	200, 300	89, 175	749, 672	19 10	271, 203	56 71
700	200, 200	152, 122	677, 660	7 20	167, 228	45 67

history was prescribed, defined by a loading time $\tau_L = 10$ s, a holding time of $\tau_H = 10$ s, and an unloading time of $\tau_U = 10$ s. In addition, a hold period of 20 s at the onset of loading facilitated the correction for any thermal drift effects in the system. A 10×10 indentation grid (100 indents) was used for all tests. For each temperature investigated, at least two different samples were grid indented (200 total indents). The specified grid spacing was 15 μm yielding a total grid surface area of 135×135 μm (approximately 0.02 mm^2). The grid spacing was chosen to be much larger than the maximum size of each phase, so that if characteristic phase sizes were larger than expected, they would not have a dominant effect on the statistical results. In other words, this large grid spacing allows statistical analysis to be used to accurately determine the properties of the individual phases.

The load–displacement data was examined in order to determine the validity of each indentation. Discontinuous load–displacement plots were observed which had a 'jump' or several 'jumps' in the indentation depth (Fig. 2, curve (b)). The cause of these jumps is uncertain, but they most likely occurred because of subsurface cracking during the force-driven indentation tests. Such cracking would explain the observed behavior: sudden increase in depth with no increase in measured load. As a result, the measured contact depth and the corresponding contact area were measured incorrectly. Most of those irregular curves are easily detectable by their greater maximum indentation depth. They can also be identified from a preliminary statistical analysis of the indentation data as Fig. 4 shows. Eliminating discontinuous indentation curves from the data set, in addition to those in violation of the scale separability condition (8), is of critical importance for accurate phase property identification.

Up to 400 °C, relatively few indentation curves were eliminated for each temperature investigated (typically less than 25%; see Fig. 4), so the number of usable results still allowed a valid statistical analysis. However, for samples exposed to higher temperatures (550 °C and 700 °C), the number of indentation curves with jumps increased dramatically, most probably due to differential shrinkage of the surface during cooling that could not be eliminated with the chosen surface preparation procedure (polishing before heating instead of after heating). As a result, an increased total number of tests needed to be carried out to obtain a large enough statistical basis of continuum indentation data. Table 2 provides a breakdown of the indentation data for each tested temperature level.

Table 3
Comparison of control specimen results (25° C) with results in the literature for unheated cement paste (mean±st.dev.): M=Indentation modulus, H=Indentation hardness, f=volume fraction

Phase	M [GPa]	H [GPa]	f [1]	Comment	Reference
LD C-S-H	21.7±2.2	–	0.66	w/c=0.5; age ~1 y	[17]
	20±2	0.8±0.2	–	w/c=0.2; C/S<1	[28]
	18.2±4.2	0.45±0.14	0.54	wcp*: w/c=0.5 age ~0.5 y	[14]
	19.1±5.0	0.66±0.29	0.77	w/c=0.5; age=28 d	Investigation
HD C-S-H	29.4±2.4	–	0.33	w/c=0.5; age ~1 y	[17]
	31±4	0.9±0.3	–	w/c=0.2; C/S>1	[28]
	29.1±4.0	0.83±0.18	0.28	wcp*=w/c=0.5 age ~0.5 y	[14]
	32.2±3.0	1.29±0.11	0.12	w/c=0.5; age=28 d	Investigation
CH	38±5	–	–	Indentation on single CH crystals	[17]
	36±3	1.35±0.5	–	–	[28]
	40.3±4.2	1.31±0.23	0.12	wcp*: deconvolution	[14]
	39.7±4.5	1.65±0.17	0.11	Deconvolution	Investigation

*Results from investigation of white cement paste.

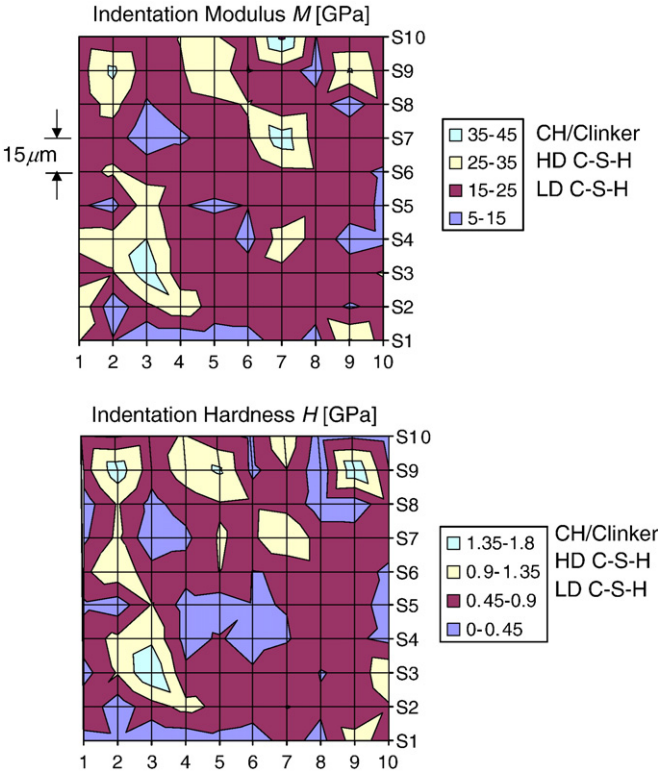

Fig. 5. Indentation stiffness and hardness maps for the control specimen. The discrete data system (M, H) is transformed in a continuous distribution of mechanical properties by linearly interpolating the nodal values over the whole indented surface (grid region). Grid spacing is 15 μm.

Table 4
Indentation modulus, hardness and C-S-H volume fraction of the three phases determined from nanoindentation indentation modulus frequency distributions (mean± st.dev.)

Temp. [°C]	Indentation modulus M [GPa]			Indentation hardness H [GPa]			C-S-H [vol. %]	
	LD C-S-H	HD C-S-H	CH/XX	LD C-S-H	HD C-S-H	CH/XX	LD	HD
25	19.1±5.0	32.2±3.0	39.7±4.5	0.66±0.29	1.29±0.11	1.65±0.17	87	19
105	18.0±5.0	29.1±4.4	–	0.68±0.29	1.33±0.17	–	74	26
200	17.8±4.7	28.4±4.1	46.3±5.5	0.79±0.32	1.66±0.28	2.44±0.06	73	27
300	14.2±5.4	25.7±6.1	40.0±8.2	0.55±0.27	1.26±0.24	1.92±0.22	76	24
400	12.4±3.6	20.3±4.4	32.1±2.8	0.42±0.16	1.00±0.26	1.93±0.51	54	46
550	9.9±3.3	17.0±3.4	28.0±7.6	0.36±0.14	0.78±0.16	1.41±0.47	77	23
700	9.3±2.6	14.5±2.1	22.3±1.3	0.27±0.08	0.58±0.12	1.10±0.13	68	32
						Average:	72±10	28

Finally, from Table 3 which compares the deconvolution results of the unheated control specimen (see Fig. 3) with results from the literature, it is readily found that our new data are in excellent quantitative agreement with previously reported indentation modulus data for all three phases considered here (LD C-S-H, HD C-S-H; CH). Some differences in hardness values can be noted, with our values being consistently higher than previous reported hardness values obtained on well hydrated white cement pastes (wcp), [14]. One possible explanation is the age of testing of our materials which was 28 days, at which (hydration) state residual clinker phases may still be dispersed throughout the material. Consistent with this explanation is the higher LD C-S-H content of our 28 days samples compared with well hydrated cement pastes. This can be grasped from the stiffness and hardness maps displayed in Fig. 5, which provide a snapshot of the hydration state of our tested material at 28 day age: high stiffness phases are rimmed by a HD C-S-H phase that can be associated with inner products, which in turn is embedded into a LD C-S-H phase (outer products) that dominates the overall response. The much harder clinker residues are expected to enhance the localized hardness response, particularly of the HD C-S-H.

Another possible explanation relates to the ordinary portland cement (OPC) paste employed in our study, which has a substantially higher volume fraction of alluminate and ferrite phases (see Table 1) than the white cement paste (wcp) tested by Costantinides and Ulm [14]. Hydrated aluminate and ferrite have been found in the outer (LD) C-S-H phase, and are known to have a higher density and to be more crystalline in nature than the C-S-H phases [19]. The presence of those dense phases may well enhance the localized hardness (and thus the strength properties) of the hydration phases, and in particular the LD C-S-H phase. Last, the CH content of 11% in our sample is consistent with the cement composition (by Bogue) of OPC having 53 wt.% of C_3S and 20 wt.% of C_2S, and is in excellent agreement with results from previous calcium leaching studies on the same material [17].

3. Nanoindentation results

The indentation modulus frequency distribution used to obtain phase results for unheated samples (25 °C) is displayed in Fig. 3. For all other investigated temperatures, similar frequency distributions were used to determine the phase properties: mean indentation modulus (M), mean indentation hardness (H), and volume fractions. The results are summarized in Table 4. The relative percentage of the two types of C-S-H, LD C-S-H and HD C-S-H, is of particular interest and is also included in Table 4. It is found not to vary in correlation with the exposure temperature, from which it can be concluded that high temperature exposure does not change the relative volume proportion of the LD C-S-H and HD C-S-H present in the material system. The difference between different samples is attributable to local variabilities of the hydration products rather than to a transformation related to

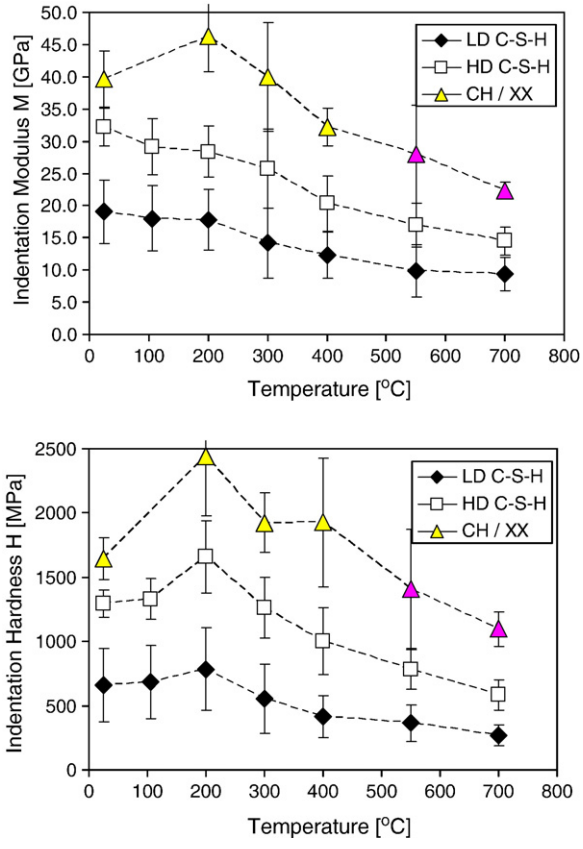

Fig. 6. Summary of nanoindentation results. Indentation modulus and Indentation hardness vs. exposure temperature for three characteristic phases: LD C-S-H, HD C-S-H, CH/XX (the XX stands for an identifiable high stiffness/hardness phase that is sensed at 550 °C and 700 °C, beyond CH dehydration). The bars at each point represent the standard deviation obtained with the deconvolution technique.

high temperature exposure. Fig. 6 displays the evolution of the indentation modulus and of the indentation hardness of each phase with respect to exposure temperature. A detailed discussion of the phase behavior found is given below.

3.1. C-S-H phases

To fully appreciate the sensitivity of the C-S-H phases with regard to temperature exposure, we plot in Fig. 7 the indentation modulus and the indentation hardness normalized by their values at 105 °C. The figure also displays, on a second axis, the weight loss rate determined by TGA. The general trend is that the nano-stiffness and the nano-hardness of the two C-S-H phases evolve in the same way, which suggests that the same chemo-physical mechanisms are at work in both the LD C-S-H phase and the HD C-S-H subjected to high temperatures. In particular, the stiffness decreases steadily but relatively slowly up to 200 °C in relation with the primary C-S-H dehydration. The increased decline of the stiffness at higher temperature cannot be attributed to the C-S-H dehydration alone, and will be discussed further later on. Furthermore, the hardness evolution of the two C-S-H phases shows an opposite trend, evidencing an increase up to 200 °C, followed by a sharp decrease. This opposite trend of stiffness vs. hardness evolution in the 100 °C to 300 °C temperature range is an indication that different mechanisms are at work as regards the effect of high temperature exposure on the elasticity properties vs. strength properties.

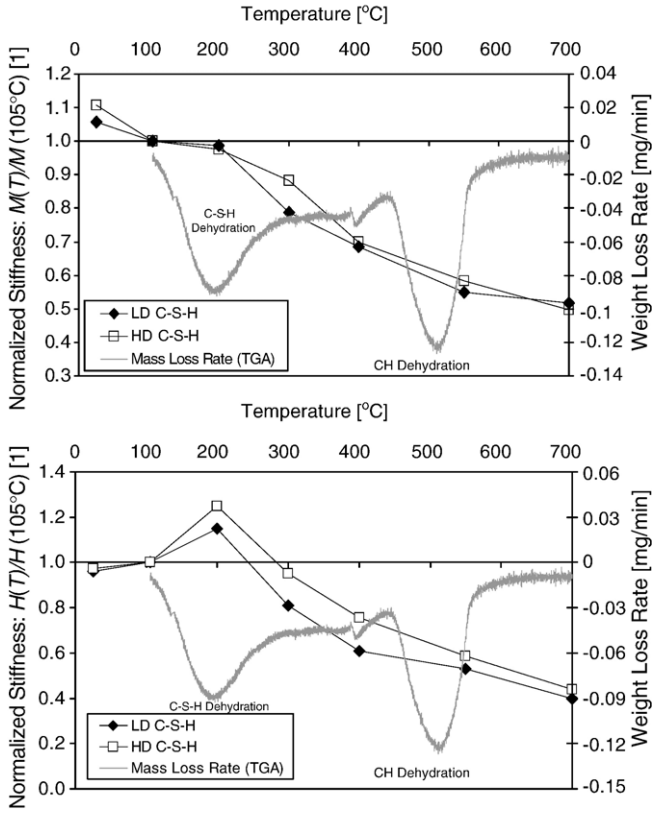

Fig. 7. Normalized stiffness and normalized hardness evolution vs. exposure temperature. The figures also display on a second axis the weight loss rate obtained from thermogravimetry.

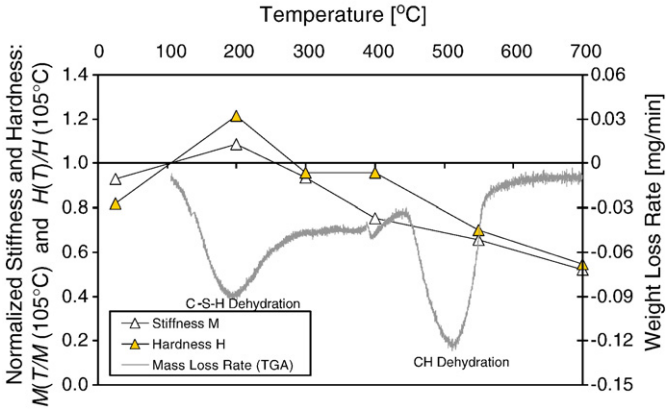

Fig. 8. Normalized stiffness and hardness evolution of the CH phase.

3.2. CH/XX phase

The effect of high temperature exposure on the CH phase was difficult to determine because CH is present in relatively small volume fractions, and instead of a clear peak in the frequency plots, the third high stiffness/hardness phase is often flatly spread out over a larger stiffness range. Nevertheless, the normalized stiffness and hardness evolution of this third phase which is displayed in Fig. 8, provides some insight into the particular effects of temperature exposure on the CH properties. In contrast to the C-S-H phases, both elasticity and hardness of CH increase up to 200 °C, before a sharp and steady decrease occurs. This particular evolution was not expected because very little dehydration is known to occur in the CH phase up to 370 °C [19]. However, initial heating could result in a more crystalline structure of the CH phase, which can be seen by the increase in stiffness and hardness at 200 °C (at 105 °C we did not find a statistically significant third phase in deconvoluting the nanoindentation data). At 550 °C and 700 °C, CH is fully dehydrated into CaO [19], which is known to be much stiffer in nature. We still find such a third high stiffness/hardness phase in the frequency plots (denoted by XX in Fig. 6); however with a stiffness that is smaller than the CH stiffness. The indentation appears not to be able to isolate the CaO properties, and the lower stiffness may well be attributed to CaO embedded in a soft C-S-H matrix.

4. Discussion

Among the key elements that allow for the assessment of the effect of high temperature exposure on the phase properties of the hydration phases is the porosity ϕ or its complimentary part the packing density, $\eta = 1 - \phi$. Unfortunately, cementitious materials have not a single porosity or a single packing mode, but at least three distinct pore spaces that are of different nature. These are from the nanoscale to the macroscale: (1) the nanoporosity (also referred to as interlayer porosity) of a characteristic size smaller than one nanometer, which separates C-S-H mineral layers; (2) the gel porosity contained in the LD and HD C-S-H gel on the order of the size of the elementary C-S-H particle, 5 nm, (3) the

capillary porosity of a characteristic size of tens to a hundred nanometers. From weighting experiments, Jennings in a number of papers (see summary in [16]) provides estimates of the different 'apparent' densities of cementitious materials at different scales, which allows one to build the following three-scale porosity model for cement paste [29,30]:

$$\phi_{tot} = (\phi_0 \eta_{LD} + \phi_{LD}) f_{LD} + (\phi_0 \eta_{HD} + \phi_{HD}) f_{HD} \phi_c \quad (9)$$

where ϕ_0 is the nanoporosity (or interlayer porosity), $\eta_{LD} = 1 - \phi_{LD}$ and $\eta_{HD} = 1 - \phi_{HD}$ are the packing density of the LD C-S-H and HD C-S-H, which occupy the relative C-S-H volume proportion f_{LD} and $f_{HD} = 1 - f_{LD}$, and ϕ_c is the capillary porosity. While f_{LD}, f_{HD} and ϕ_c depend on mix proportions (namely on the w/c ratio, the hydration degree, etc.), both the nanoporosity ϕ_0 and the gel packing densities η_{LD} and η_{HD} do not vary from one cementitious material to another. In particular, from the density values provided by Jennings [16] for saturated and dry C-S-H, it is straightforward to estimate the nanoporosity ($\phi_0 = 0.18$) and respectively the C-S-H sheet packing density ($\eta_s = 1 - \phi_0 = 0.82$) [29]. Similarly, the packing density of the LD C-S-H and HD C-S-H is found to be $\eta_{LD} = 0.63$ and $\eta_{HD} = 0.76$. These two packing densities almost coincide with *limit* packing densities of spheres. The LD C-S-H packing density almost coincides with the random packing density of spheres of $\eta \approx 0.64$, which corresponds to the maximum packing density in the random close-packed limit (known as RCP) [31,33]. On the other hand, the HD C-S-H packing density almost coincides with the densest possible spherical packing in three-dimensions of $\eta = \pi/\sqrt{18} \approx 0.74$ [32], which is the ordered face-centered cubic (fcc) or hexagonal close-packed (hcp) packing. The question that here arises is how those packing densities (or porosities) evolve with high temperature exposure?

4.1. Link with Mercury Intrusion Porosimetry (MIP) studies

To fully appreciate the question, it is instructive to briefly review results from Mercury Intrusion Porosimetry (MIP) studies of the change of porosity (respectively packing density) due to high temperature exposure [7,5]. It should be noted that MIP allows access to pore diameters ranging from 3 nm to 375 μm depending on the apparatus [34]. This allows access to the capillary porosity (ϕ_c), but the gel porosities of both LD and HD C-S-H, ϕ_{LD} and ϕ_{HD}, are just at the limit of this investigation technique. It is likely that MIP can access the LD C-S-H gel porosity (ϕ_{LD}), but not the HD C-S-H gel porosity (ϕ_{HD}). MIP studies of the effect of high temperature on the pore structure show that the porosity increases only slightly up to 200 °C and is basically constant between 200 °C and 300 °C. Komonen et al. [7] also noted that the increase of total pore volume up to 300 °C was significantly less than could be expected by weight loss measurements (which agrees with investigations on mortar [35]). On the other hand, between 300 °C and 400 °C, MIP results indicate that the C-S-H gel porosity (<10 nm pore diameter, most probably ϕ_{LD}) increases significantly. While the gel porosity continues to increase between 400 °C and 550 °C, MIP provides evidence of a concurrent increase in larger pore diameters (40–100 nm pore diameter) as well. This increase in larger pore diameters is most likely due to the decomposition of CH, creating an additional capillary porosity; but it could also be a result of an increase in the average size of the gel pores. This increase of large pores dominates between 550 °C and 700 °C, while the smaller gel pores undergo almost no change.

The MIP results hint towards the concurrent existence of two mechanisms that possibly drive the high temperature evolution of the C-S-H phases: (1) an intrinsic dehydration of the C-S-H particles which should give rise to a correlation between mass loss and C-S-H particle properties, particular for temperatures <300 °C, and (2) a change in the gel porosities (ϕ_{LD}, ϕ_{HD}), i.e. the C-S-H packing densities (η_{LD}, η_{HD}) for temperatures above 300 °C. The focus of the next two sections is to develop a means to identify and possibly quantify those two mechanisms using our nanoindentation results.

4.2. Hypothesis I: C-S-H dehydration

Let us first assume that dehydration was the sole source of the high temperature degradation of the C-S-H elasticity, and that the packing densities of the LD and HD C-S-H were not affected by high temperature exposure. Testing this hypothesis shows that there may well be some evidence in favor of this assumption up to 300 °C, but that it cannot explain the thermal C-S-H degradation for higher exposure temperatures.

Direct experimental measurement of the nanomechanical properties of the C-S-H solid particles is still out of reach, and indeed the only measurable properties by nanoindentation are the properties of the LD C-S-H and HD C-S-H *composites*, which comprise the solid particle and the gel porosities. From density, composition, and surface area measurements, Jennings [15,16] postulates a globular C-S-H particle morphology of characteristic size 5.6 nm (which includes the $\phi_0 = 18\%$ nanoporosity). At larger scales, those globular particles agglomerate to form a Low Density (LD) and a High Density (HD) C-S-H 'gel', that differ only in the packing density η_{LD} and η_{HD}. Not surprisingly, as the packing density increases, the mechanical properties (M, H) increase as well. However, as recently shown [14], the indentation stiffness (as well as the hardness) of the two C-S-H phases, LD C-S-H and HD C-S-H, of unheated cement paste scale with the packing density along a straight line that yields a zero stiffness for a packing density of the C-S-H particles of $\eta \sim 0.5$ (percolation threshold). The very existence of this solid percolation threshold is a unique hallmark of granular materials [31]. Indeed, from granular mechanics it is known that a granular assembly becomes unstable below the random loose-packed limit (RLP) of $\eta = 0.56$, which corresponds to the loosest packing of spheres for which a continuous force path can be established. Furthermore, from continuum micromechanics [36,37], or more precisely micro-poromechanics [38–40], it is known that a material exhibiting a packing percolation threshold $\eta_0 = 0.5$, corresponds to a polycrystal material, a perfectly disordered solid phase intermixed with some porosity [41]. The polycrystal or self-consistent model (SC) provides a means to evaluate the link between the composite indentation modulus M and the solid's elastic modulus m_s. In

particular, for a solid's Poisson ratio $v_s = 0.2$, the SC-model yields a linear scaling of M with the packing density η [14]:

$$\frac{M}{m_s} = 2\eta - 1 \tag{10}$$

The SC-model is the background for the analysis of our experimental results. In particular, as shown in Fig. 9(a), the fitting of a straight line through the 25 °C LD and HD C-S-H indentation modulus values for the reference *limit* packing densities, $\eta_{LD} \approx 0.64$ and $\eta_{HD} \approx 0.74$, readily confirms the 'nano-granular' behavior of the two C-S-H phases, i.e. the percolation threshold $\eta = 0.5$, and the C-S-H solid particle stiffness ms (25 °C) = M ($\eta = 1$, 25 °C) ≈ 65 GPa.

This simple micromechanics model lends itself readily for hypothesis testing. Indeed, if dehydration was the sole source of the thermal degradation, the only property that should change is the solid's particle stiffness m_s (T), while the packing densities of the two C-S-H phases would remain at their reference *limit* values $\eta_{LD} \approx 0.64$ and $\eta_{HD} \approx 0.74$ for all investigated temperatures. The straight line fits in Fig. 9(a) are based on this assumption. For each temperature, the asymptotic solid particle stiffness m_s (T) = M ($\eta = 1$, T) was determined by extrapolating the M–η scaling relations in Fig. 9(a) to $\eta = 1$ for all tested temperatures. Furthermore, if dehydration of the C-S-H particles was indeed the sole source of the thermal damage of the C-S-H phases, the asymptotic particle stiffness m_s (T) should strongly correlate with the (independently) measured mass loss. The results are shown in Fig. 9(b) in a plot of m_s (T) vs. mass normalized by its value at 105 °C. There is indeed a very good correlation of m_s (T) with the mass loss due to dehydration up to 300 °C, for which values align along a straight line; thus hinting towards a role of dehydration in the thermal damage of the C-S-H properties. The change in the solid's stiffness in the temperature range 105 °C–300 °C, however, is rather small, <5%, which may well be statistically insignificant. Furthermore, Fig. 9(b) provides strong evidence of a second mechanism at play above 300 °C, for which the assumption of a constant packing density poorly correlates with the mass evolution. In other words, it is very unlikely that C-S-H dehydration is the sole source of C-S-H stiffness degradation.

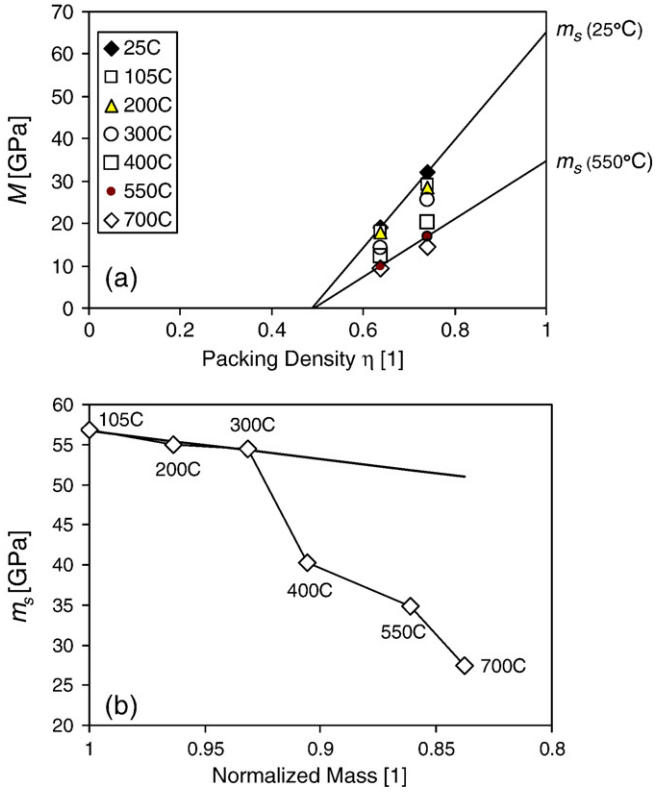

Fig. 9. C-S-H dehydration assumption (Hypothesis I). (a) Indentation modulus-packing density scaling relation (M–η), established under the assumption of fixed packing densities; (b) extrapolated C-S-H particle stiffness $m_s = M$ ($\eta = 1$) vs. normalized mass (normalized by mass at 105 °C).

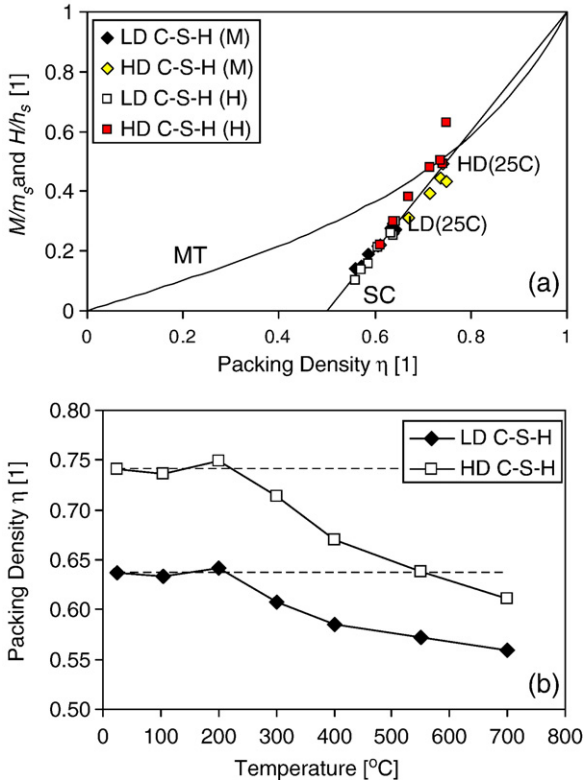

Fig. 10. Back-analysis of the packing density of LD C-S-H and HD C-S-H subjected to high temperatures established under the assumption of constant particle properties (Hypothesis II). (a) Normalized indentation modulus and normalized hardness relations vs. particle packing density. (b) Particle packing density vs. exposure temperature.

4.3. Hypothesis II: change in C-S-H packing density

Let us next assume that change in C-S-H packing density was the sole source of the thermal degradation of the mechanical nanoproperties. Testing this hypothesis requires the determination of the packing densities of LD C-S-H and HD C-S-H as functions of the temperature, while the mechanical properties of the solid's particle are fixed for all temperatures. In a first approach, this is achieved by minimizing the quadratic error

between the experimental values (M_i, H_i) and the linear scaling model (10) applied to both indentation modulus and indentation hardness:

$$\min_{(m_s,h_s),\eta_i} \sum_{i=1}^{n} \left[(M_i(T), H_i(T)) - (m_s, h_s)(2\eta_i - 1)\right]^2 \tag{11}$$

$$\text{s.t.} \begin{cases} \eta_{LD}(25\ ^\circ\text{C}) = 0.64 \\ \eta_{HD}(25\ ^\circ\text{C}) = 0.74 \\ \eta_i \geq 0.5 \end{cases}$$

Herein, $M_i = M\ (T_i)$ and $H_i = H\ (T_i)$ are the $2n$ experimental modulus and hardness values of the LD C-S-H and HD C-S-H determined by nanoindentation (Table 4); $m_s = M\ (\eta = 1)$ and $h_s = H\ (\eta = 1)$ are the unknown stiffness and the hardness of the C-S-H particle, which are assumed to be temperature independent; and finally $\eta_i = \eta\ (T_i)$ ($i = 1, n$) are the unknown packing densities of LD C-S-H and HD C-S-H. The linear scaling model of the indentation modulus is motivated by the micromechanics model (10), which assumes a temperature insensitive Poisson's ratio of the C-S-H particle, $\nu_s = 0.2$. The linear scaling of the hardness with the packing density is a first-order modeling attempt to scale the strength of the nanogranular particles by their density (for a refined model, see [42]). The optimization problem (11) which is constrained by the reference *limit* packing densities, is well defined: $2n+2$ experimental input values contrast $n+2$ output values. The results of error minimization are shown in Fig. 10(a) which shows the normalized modulus M/m_s and normalized hardness H/h_s vs. the packing density η. As expected, all values align along a straight line defined by the particle percolation threshold $\eta_0 = 0.5$ that characterizes the nanogranular morphology. The particle stiffness and particle hardness values, assumed temperature insensitive, are $m_s = 65.4$ GPa and $h_s = 2.6$ GPa. It is tempting to compare the particle properties with the mechanical properties recently obtained from atomistic simulations. From energy minimization at 0 K, Pellenq and van Damme [44] reported the mean Young's modulus of Hamid's structure (C/S = 1) to be $E_s = 57.1$ GPa, which compares fairly well with the Young's modulus we calculate from $E_s = m_s\ (1 - \nu_s^2) = 63.3$ GPa.

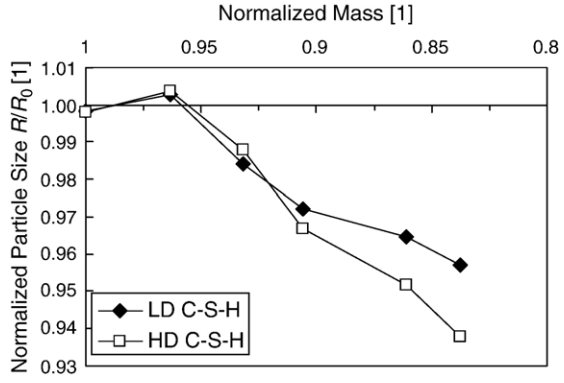

Fig. 11. Normalized C-S-H particle radius determined from the packing density ($R/R_0 = (\eta\ (T_i)/\eta_0)^{1/3}$) vs. normalized mass (normalized by mass at 105 °C). The change in radius provides evidence of a C-S-H particle shrinkage.

Furthermore, for comparison, Fig. 10(a) also displays the normalized indentation modulus/hardness curve for a matrix-pore inclusion morphology which is represented in micromechanics by the Mori-Tanaka scheme (MT) [43], and for which for $\nu_s = 0.2$ [29]:

$$\frac{M}{m_s} = \frac{\eta}{2-\eta} \tag{12}$$

In contrast to the self-consistent model (SC) employed in Eq. (11), the MT model (12) does not allow fitting the C-S-H indentation data (M_i, H_i) for constant values of m_s and h_s; thus providing further evidence that C-S-H particles behave *in situ* like a nanogranular material rather than a matrix-pore inclusion material. Comprised of the same solid particle (same m_s and h_s), the change in the mechanical performance of C-S-H is primarily scaled by the packing density. This is exemplified in Fig. 10(b) which displays the packing density values $\eta_i = \eta\ (T_i)$ obtained from Eq. (11) for LD C-S-H and HD C-S-H. Under the assumption of temperature insensitive particle properties, the packing densities is found to be almost constant for exposure temperatures up to 200 °C. Above 200 °C, the packing density significantly decreases, and reaches for the LD C-S-H phase at 700 °C a value that is close to the loose-packed limit (RLP) of $\eta = 0.56$ [31].

5. Conclusions

In this paper, the driving forces for the thermal degradation of the nanostiffness and nanostrength properties of C-S-H in cementitious materials are discussed. To our knowledge, previous contributions to the topic focussed on the dehydration mechanism. Based on an original nanoindentation technique and micromechanics analysis, a new mechanism is identified: a thermally induced change of the packing density of C-S-H particles, which appears to be the dominant mechanism driving the thermal degradation of C-S-H in cementitious materials:

1. The nanoindentation results and micromechanics analysis confirm the existence of two structurally distinct but compositionally similar C-S-H phases heretofore hypothesized to exist as Low Density (LD) C-S-H and High Density (HD) C-S-H [15,16], or outer and inner products [27]. Both phases exhibit a unique nanogranular behavior, that is a behavior driven by particle-to-particle contact forces rather than by mineral properties. We confirm that both phases, LD and HD C-S-H, are composed of the same elementary building block, the C-S-H particle (or globuli in Jennings terminology [16]). From granular mechanics, it is known that the packing density relates to the number of contact points [33]. Since both C-S-H phases are made of the same particle, the higher stiffness of the HD C-S-H compared to LD C-S-H, therefore, is attributable to the greater number of contact points that stabilize the C-S-H particle.
2. The significant dehydration of the C-S-H particle that occurs between 105 and 300 °C (Fig. 1) does not translate into a significant change of the particle stiffness (Fig. 9(b)). Furthermore, up to 200 °C, the packing densities of C-S-H are found to be almost constant (Fig. 10(b)). These observations are

consistent with MIP results that show a poor match between weight loss measurements and porosity change up to 300 °C [7]. From a granular mechanics point of view, the insignificant change of the packing densities means that the number of particle-to-particle contact remains unchanged.

3. The main thermal deterioration of the C-S-H gel properties, which occurs above 200 °C, is attributable to a change of the packing density of C-S-H particles (Fig. 10), while the particle properties remain unchanged. The chemo-physical origins of this loss of C-S-H packing density still remain to be discovered. It may well be related to the dehydration of C-S-H particles which are expected to shrink [45] thus reducing the number of contact points with neighboring particles. An estimate of this particle shrinkage can be obtained by dividing the LD and HD C-S-H packing densities $\eta\ (T_i)$ by their respective reference *limit* packing densities, η_{LD} (25 °C) ≈ 0.64 and η_{HD} (25 °C) ≈ 0.74. In a first approximation, considering a spherical particle shape, the change in radius of the particles $R/R_0=(\eta\ (T_i)/\eta_0)^{1/3}$ can be assimilated with the shrinkage. Fig. 11 plots R/R_0 vs. mass normalized by its value at 105 °C. For both LD C-S-H and HD C-S-H we find a linear decrease of R/R_0 with the decrease in mass for temperatures above 200 °C. It is interesting to note that a maximum particle shrinkage of $R/R_0-1\approx-5\%$ at 700 °C suffices to reduce the packing density of LD C-S-H close to the loose-packed limit (RLP) of $\eta=0.56$. The shrinkage of the C-S-H particle, therefore, appears to us a prime candidate to explain the change in packing density of the C-S-H phases, which ultimately entails the thermal deterioration of cementitious materials.

Acknowledgements

The authors gratefully acknowledge the Lafarge Group for providing the financial support for this research with Jean-François Batoz as Technical Advisor and Dr. Paul Acker as Scientific Advisor. The authors also thank Alan Schwartzman, director of the NanoMechanical Laboratory at MIT, Dr. Georgios Constantinides and Chris Bobko for their assistance with indentation testing, and Dr. John T. Germaine for his assistance with specimen preparation and laboratory testing.

References

[1] F.-J. Ulm, P. Acker, M. Lévy, The "Chunnel" fire. II: Analysis of concrete damage, Journal of Engineering Mechanics, ASCE 125 (3) (1999) 283–289.
[2] A. Khennane, G. Baker, Plasticity models for the biaxial behavior of concrete at elevated temperatures, Computational Methods of Applied Mechanics and Engineering 100 (1992) 207–223.
[3] K. Willam, I. Rhee, Y. Xi, Thermal degradation of heterogeneous concrete materials, Journal of Materials in Civil Engineering, ASCE 17 (3) (2005) 276–285.
[4] W.P.S. Dias, G.A. Khoury, P.J.E. Sullivan, Mechanical properties of hardened cement paste exposed to temperatures up to 700 C (1292 F), ACI Materials Journal 87 (2) (1990) 160–166.
[5] M.C.R. Farage, J. Sercombe, C. Galle, Rehydration of microstructure of cement paste after heating at temperatures up to 300 °C, Cement and Concrete Research 33 (2003) 1047–1056.
[6] S. Masse, G. Vetter, P. Boch, C. Haehnel, Elastic modulus changes in cementitious materials submitted to thermal treatments up to 1000 °C, Advances in Cement Research 14 (4) (2002) 169–177.
[7] J. Komonen, V. Penttala, Effects of high temperature on the pore structure and strength of plain and polypropylene fiber reinforced cement pastes, Fire Technology 39 (2003) 23–34.
[8] Z.P. Bažănt, M.F. Kaplan, Concrete at High Temperatures: Material Properties and Mathematical Models, Longman, London, England, 1996.
[9] F.-J. Ulm, O. Coussy, Z.P. Bazănt, The "Chunnel" fire. I: Chemoplastic softening in rapidly heated concrete, Journal of Engineering Mechanics, ASCE 125 (3) (1999) 272–282.
[10] T.Z. Harmathy, Thermal properties of concrete at elevated temperatures, ASTM Journal of Materials 5 (1) (1970) 47–74.
[11] T.Z. Harmathy, Fire Safety Design and Concrete, Longman, London, England, 1993.
[12] W.-M. Lin, T.D. Lin, L.J. Powers-Couche, Microstructure of fire-damaged concrete, ACI Materials Journal 93 (3) (1996) 199–205.
[13] S.K. Handoo, S. Agarwal, S.K. Agarwal, Physicochemical, mineralogical, and morphological characteristics of concrete exposed to elevated temperatures, Cement and Concrete Research 32 (2002) 1009–1018.
[14] G. Constantinides, F.-J. Ulm, 'The nanogranular nature of C-S-H.' Journal of the Mechanics and Physics of Solids, In Press (available online Sept. 1, 2006).
[15] P.D. Tennis, H.M. Jennings, A model for two types of calcium silicate hydrate in the microstructure of portland cement pastes, Cement Concrete Research 30 (2000) 855–863.
[16] H.M. Jennings, Colloid model of C-S-H and implications to the problem of creep and shrinkage, Materials and Structures (Special issue of Concrete Science and Engineering) 37 (265) (2004) 59–70.
[17] G. Constantinides, F.-J. Ulm, The effect of two types of C-S-H on the elasticity of cement-based materials: results from nanoindentation and micromechanical modeling, Cement Concrete Research 34 (1) (2004) 67–80.
[18] W.W. Wendlandt, Thermal Analysis, 3rd Edition, John Wiley & Sons, Inc., New York, USA, 1986.
[19] H.F.W. Taylor, Cement Chemistry, 2nd Edition, Thomas Telford, London, England, 1997.
[20] W.C. Oliver, G.M. Pharr, Measurement of hardness and elastic modulus by instrumented indentation: advances in understanding and refinements to methodology, Journal of Material Research 19 (2004) 3–20.
[21] Y.-T. Cheng, C.-M. Cheng, Scaling, dimensional analysis and indentation measurements, Materials Science & Engineering. Reports 44 (2004) 91–149.
[22] W.C. Oliver, G.M. Pharr, An improved technique for determining hardness and elastic modulus using load and displacement sensing indentation experiments, Journal of Materials Research 7 (6) (1992) 1564–1583.
[23] L.A. Galin, in: I.N. Sneddon (Ed.), Contact Problems in Theory of Elasticity, North Carolina State College, 1961, Translated by H. Moss.
[24] I.N. Sneddon, The relation between load and penetration in the axi-symmetric Boussinesq problem for a punch of arbitrary profile, International Journal of Engineering Science 3 (1965) 47–57.
[25] F.P. Ganneau, G. Constantinides, F.-J. Ulm, Dual-indentation technique for the assessment of strength properties of cohesive-frictional materials, International Journal of Solids and Structures 43 (4) (2006) 1727–1745.
[26] A. Nonat, The structure and stoichiometry of C-S-H, Cement Concrete Research 34 (2004) 1521–1528.
[27] I.G. Richardson, Tobermorite/jennite- and tobermorite/calcium hydroxide-based models for the structure of C-S-H: applicability to hardened pastes of tricalcium silicate, β-dicalcium silicate, Portland cement, and blends of Portland cement with blast-furnace slag, metakaolin, or silica fume, Cement Concrete Research 34 (2004) 1733–1777.
[28] P. Acker, Micromechanical analysis of creep and shrinkage mechanisms, in: F.-J. Ulm, Z. Bažant, F. Wittman (Eds.), Creep, Shrinkage and Durability Mechanics of Concrete and other Quasi-Brittle Materials, Elsevier, Oxford, UK, 2001, pp. 15–25.
[29] F.-J. Ulm, G. Constantinides, F.H. Heukamp, Is concrete a poromechanics material? — A multiscale investigation of poroelastic properties, Materials and Structures (Special issue of Concrete Science and Engineering) 37 (265) (2004) 43–58.
[30] F.-J. Ulm, A. Delafargue, G. Constantinides, Experimental Microporomechanics, in: L. Dormieux, F.-J. Ulm (Eds.), Applied Micromechanics of

Porous Materials, CISM Courses and Lectures, vol. 480, Springer, Wien New York, 2005, pp. 207–288.
[31] H.M. Jaeger, S.R. Nagel, Physics of granular state, Science 255 (5051) (1992) 1523–1531.
[32] N.J.A. Sloane, Kepler's conjecture confirmed, Nature 395 (1998) 435–436.
[33] A. Donev, I. Cisse, D. Sachs, E.A. Variano, F.H. Stillinger, R. Connely, S. Torquato, P.M. Chaikin, Improving the density of jammed disordered packings using ellipsoids, Science 303 (2004) 990–993.
[34] C. Galle, Effect of drying on cement-based materials pore structure as identified by mercury intrusion porosimetry: a comparative study between oven-, vacuum-, and freeze-drying, Cement and Concrete Research 31 (2001) 1467–1477.
[35] R.S. Rostasy, R. Weiss, G. Weidemann, Changes of pore structure of cement mortars due to temperature, Cement and Concrete Research 10 (2) (1980) 157–164.
[36] P. Suquet (Ed.), Continuum Micromechanics, CISM Courses and Lectures, vol. 377, Springer Verlag, WienNew York, 1997.
[37] A. Zaoui, Continuum micromechanics: survey, Journal of Engineering Mechanics, ASCE 128 (8) (2002) 808–816.
[38] L. Dormieux, A. Molinari, D. Kondo, Micromechanical approach to the behaviour of poroelastic materials, Journal of the Mechanics and Physics of Solids 50 (2002) 2203–2223.
[39] L. Dormieux, F.-J. Ulm (Eds.), Applied micromechanics of porous materials, CISM Courses and Lectures, vol. 480, Springer, Wien New York, 2005.
[40] L. Dormieux, J. Kondo, F.-J. Ulm, Microporomechanics, J. Wiley, Chichester, UK, 2006.
[41] E. Kröner, Statistical Continuum Mechanics, CISM Courses and Lectures, vol. 92, 1971 Udine, Italy.
[42] S. Cariou, F.-J. Ulm, L. Dormieux, (2006), The effect of the packing density on the indentation hardness of cohesive-frictional porous materials, J. Mech. Phys. Solids, In Review.
[43] T. Mori, K. Tanaka, Average stress in matrix and average elastic energy of materials with misfitting inclusions, Acta Metallurgica 21 (5) (1973) 571–574.
[44] R.J.M. Pellenq, H. Van Damme, Why does concrete set?: The nature of cohesion forces in hardened cement-based materials, MRS Bulletin 29 (5) (2004) 319–323.
[45] W.P.S. Dias, G.A. Khoury, P.J.E. Sullivan, Shrinkage of hardened cement paste at temperatures up to 670 C (1238 F), ACI Materials Journal 87 (3) (1990) 204–209.